On the modelling of highly anisotropic diffusion for electron radiation belt dynamic codes

Nour Dahmen, François Rogier, Vincent Maget

On the modelling of highly anisotropic diffusion for electron radiation belt dynamic codes

Nour DAHMEN[a,*], François ROGIER[b], Vincent MAGET[a]

[a] *ONERA/DPHY, Université de Toulouse, Toulouse, France*
[b] *ONERA/DTIS, Université de Toulouse, Toulouse, France*

Abstract

Electron radiation belts are regions surrounding Earth, filled with highly energetic electrons and overlapping the majority of satellite orbits. Their multi-scale and rapidly evolving dynamics are modelled by the mean of a diffusion equation involving a highly anisotropic and inhomogeneous diffusion tensor. Finite difference based methods have been the preferred method of discretization in physical codes, starting from ONERA's *Salammbô*-Electron model, the pioneering 3-dimensional code in the radiation belts community. This choice however does not prevent several numerically induced constraints impacting the reliability of the code as well as its computational cost. Thus in this paper we present the outcome of our investigation to improve Salammbô's numerical core. In particular, we present our special diffusion frame and its numerically induced limitations on our finite difference based scheme. Then we test potential alternative finite volume schemes with physically relevant properties and we finally highlight with a real case simulation the contribution of the positivity preserving scheme to evaluate the impact

*Corresponding author.
E-mail address: nourallah.dahmen@onera.fr

of cross diffusion.

Keywords: Radiation belts; Finite volume method; Anisotropic diffusion equation; Monotony; Discrete maximum principle.

---

1. Introduction

Earth's space environment is a vast dynamic region extending from the upper atmosphere to the interplanetary region. It is constantly disrupted by charged particles, piled up in plasmas and originating from the Sun's activity. Highly energetic electrons and protons injected near Earth especially, are trapped by the Earth's magnetic field. They form quasi permanent toroidal structures called radiation belts or Van Allen belts [1].

Radiation belts (One proton belt, and two electron belts separated by the Slot region) are located between 700 km and 58000 km of altitudes (Figure 1) and they span the majority of satellite orbits [2]. Due to the trapped particles energy magnitudes (between 100 keV to 10 MeV for electrons) in addition to rapidly varying particle fluxes, satellites crossing them can undergo severe damages on their on-board equipments and their thermal shielding [2]. Thus, to ensure a reliable design for spacecraft, radiation belts require faithful models and a precise understanding of their underlying mechanisms.

The practical difficulty of conducting precise in-situ measurements, and the complexity of understanding several multi-physics drivers, prevents the construction of a unique modelling instrument. Thus, the radiation belts community relies on an arsenal of tools, including empirical models, statistical models and physical codes [3]. Precisely, the latter have imposed themselves as reliable implements. They are derived from a theoretical approach

of the radiation belt dynamics and benefit from the improvement of the physical processes comprehension in addition to more refined measurement data [3].

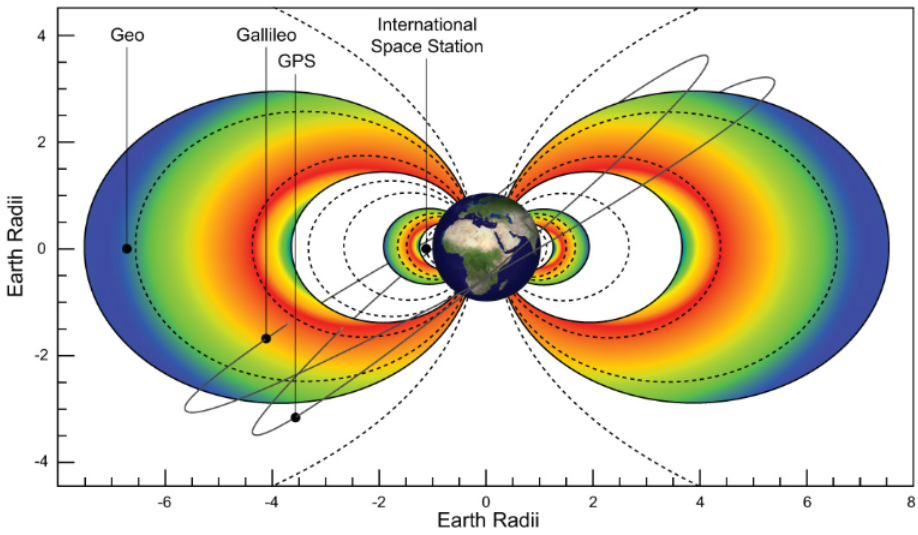

Figure 1: Inner and outer electron radiation belts extending over several satellite orbits, reproduced from [2]

The theoretical development of physical codes, as described in [4], is founded on the adiabatic invariants theory. Each trapped particle's motion can be decomposed and associated into 3 conserved quantities or adiabatic invariants [5]. Using a Hamiltonian formalism on a Boltzmann equation and introducing a Fokker Planck operator to evaluate physical interactions responsible for changing particles trapping state, a 3-dimensional transient diffusion equation is obtained (in the adiabatic invariant phase space).

The near majority of physical codes related to electron radiation belts, starting from ONERA's *Salammbô*-Electron code [6], along with *Versatile*

Electron Radiation Belt Code VERB [7], *Storm-Time Evolution of Electron Radiation Belt* Code STEERB [8] and the *British Antarctic Survey* (BAS) Radiation Belt model code [9] solve numerically the diffusion equation using a finite difference (FD) based method. However, they differentiate on the temporal integration methods. While VERB,and BAS are fully implicit, *Salammbô*-Electron is explicit and STEERB uses the Alternating Direction Implicit (ADI) scheme. They also adopt different numerical grid rendering strategies. These differences are mainly motived by computing time optimization, numerical stability arguments, and locally sought accuracy [7][8][9][10]. During the simulation, the numerical resolution is usually correlated to volatile time dependent empirical parameters reflecting the dynamics of the system induced by solar activity. The main proxy for such models is the geomagnetic activity index named Kp and we report in figure 2 an example of its temporal evolution.

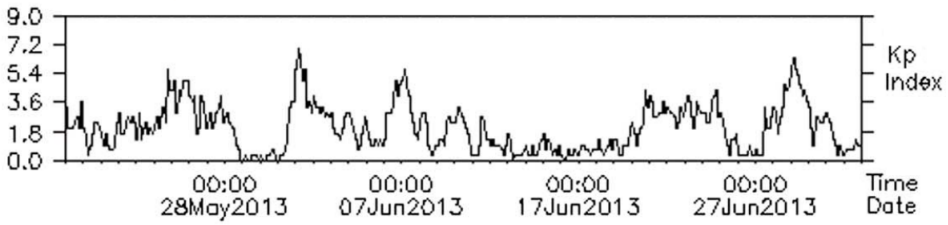

Figure 2: Kp index time evolution for 1 month reproduced from [11]

Nevertheless, the numerical resolution of this particular diffusion equation is not straightforward and many challenges need to be tackled. First, the studied diffusion is very inhomogeneous, involving diffusion coefficients with steep spatial evolutions. Second, the diffusion achieves high levels of

anisotropy, amplified by cross diffusion terms. When retained, they induce severe numerical instabilities and their presence in the diffusion frame is a subject of study and discussion. These intense aspects impose huge limitations on the numerical stability and generate approximations with a non physical behavior [12].

Thus, this paper yields the results of the investigation undertaken to rearrange *Salammbô*-Electron numerical core. From the large panel of numerical schemes, the choice of the new appropriate method has to be motivated by its expected properties and the system constraints. FD methods were usually favoured among the community due to their ease of implementation. They has shown however their limit to contain non-physical numerical deviations. In fact important properties of positivity and discrete Minimum/Maximum principles are not preserved. Continuous finite element methods, on the other hand have been extensively studied for parabolic equations and applied to diffusion problems [13]. They satisfy the energy conservation and offer important robustness properties. But apart some particular cases, the Min/Max preserving property is not ensured and strong variations of diffusion coefficients are not well taken into account. Extension to high order and discontinuous coefficients has been reached recently in the frame of Discontinuous Galerkin Method (DGM) [14]. Hereby we consider fundamental for the new scheme to be adopted, to maintain a physically relevant solution, and we choose to work with Finite Volume (FV) based methods (that can be considered as a DGM of lowest order). First, they provide the flux conservation property, particularly important to conservation laws like diffusion. Besides, positivity preserving and Minimum/Maximum principle preserving

FV variants exist [15] and have been tested for reservoir engineering applications [16].

This paper is organized as follows : Section 2 is devoted to the presentation of the general 3D diffusion frame in radiation belts and the numerically challenging 2D diffusion case that retain most of the numerical constraints that we were interested in. Then we present some aspects of the implementation in *Salammbô-Electron*. We also present qualitatively some of the overriding aspects of the studied diffusion and their induced constraints. Section 3 is related to explaining the methodology we followed to identify alternative schemes, suitable for our application. In particular, we present two FV schemes, a non-linear monotone FV scheme and a non-linear extremum preserving FV scheme. We show later several numerical test results of both schemes, solving a steady state diffusion problem with real life mimicking conditions. Section 4 then presents a transient diffusion study case involving a "physical" diffusion tensor with the aim to compare both schemes on the computational cost side for different time steps. We compare the simulations results of a typical FD and the monotone non-linear scheme, and evaluate the effect of cross diffusion in the case of the latter scheme. Finally Section 5 summarizes and concludes our work.

2. Electron Radiation belt dynamics modelling : a typical diffusion problem but many challenges due to harsh environment

2.1. A multi scale diffusion problem

The evolution of the Phase Space Density (PSD) function f, picturing the statistical distribution of trapped electrons, is expressed in the following

3 dimension diffusion equation in its canonical form :

$$\frac{\partial f}{\partial t} = \sum_{i=1}^{3}\sum_{j=1}^{3} \frac{\partial^2}{\partial J_i \partial J_j}(D_{J_i J_j} f) \tag{1}$$

where t is time, J_1, J_2, J_3, the three adiabatic invariants, and $D_{J_i J_j}$ for $i, j \in \{1,2,3\} \times \{1,2,3\}$ the diffusion coefficients. The first and second invariant J_1, J_2 are highly coupled, while J_3 is decoupled from the two first invariants [17]. This can be seen in the different characteristic time scales τ_1, τ_2, τ_3 associated respectively to J_1, J_2, J_3 reported in table 1. This aspect, among other assumptions, leads to a diffusion tensor without cross-diffusion terms associating the J_3 direction ($D_{J_1 J_3} = D_{J_2 J_3} = D_{J_3 J_2} = D_{J_3 J_1} = 0$).

Table 1: Magnitude time of the decomposed motions of trapped electrons, at different energies and altitudes.

2000 Km	τ_1 (s)	τ_2 (s)	τ_3 (s)
E = 50 keV	$2.5 \cdot 10^{-6}$	0.25	41400
E = 1 MeV	$7 \cdot 10^{-6}$	0.1	3180

13000 Km	τ_1 (s)	τ_2 (s)	τ_3 (s)
E = 1 MeV	$1 \cdot 10^{-2}$	1	1020

The latter equation, is usually transformed and solved in the (y,E,L^*) space [18] where :

- $y = \sin(\alpha_{eq})$ with α_{eq} the particle's equatorial pitch angle, the angle between its velocity vector and the magnetic field at the equator.

- E is the particle's kinetic energy, expressed in eV.
- L^* is the radial distance at the equator of the field line (dipole approximation) travelled by the trapped particle, from the center of Earth [5], expressed in Earth's radii .

This transformation allows the representation of the PSD function f in a more tangible space, rather than the abstract adiabatic invariants space, and permits a convenient estimation of the physical diffusion terms : D_{EE},D_{yy},D_{yE} and $D_{L^*L^*}$.

Same as in the invariant space for J_3, the radial diffusion (i.e. diffusion along the L^* direction) is decorrelated and operates on a global scale. It originates from magnetic and electric perturbations [4] and is responsible for shifting injected particles in the outer boundary at L^*_{max} toward Earth. On the other hand, diffusion occurring in the (y, E) plane operates on a local scale. D_{EE}, D_{yy} and D_{yE} terms embody the effects of resonant wave-particle and particle-particle interactions [18]. They are sensitive to the various diffusion mediums crossed by the trapped electron, characterized by abrupt transitions due to an uneven distribution of different types of plasma waves (with different amplitudes and resonance frequencies). They are mainly responsible for scattering electrons into the loss cone, the inner boundary of the radiation belt at y_{min}, modelling electron loss due to atmospheric precipitations.

Thereby, the 3D diffusion equation is usually solved separately between these two sets of diffusions [7][8][9]. In this paper, we will focus, on the much more numerically challenging 2D diffusion occurring in the (y, E) plane, reported in equation (2).

$$\begin{aligned}\frac{\partial f}{\partial t} =& \frac{1}{G}\frac{\partial}{\partial y}|_{y,L^*}(G(D_{yy}\frac{\partial f}{\partial y}|_{E,L^*} + D_{yE}\frac{\partial f}{\partial E}|_{y,L^*}))+ \\ & \frac{1}{G}\frac{\partial}{\partial E}|_{E,L^*}(G(D_{EE}\frac{\partial f}{\partial E}|_{y,L^*} + D_{yE}\frac{\partial f}{\partial y}|_{E,L}))\end{aligned} \tag{2}$$

G is the Jacobian of the $(J_1, J_2) \rightarrow (y, E)$ transformation. A conservative form of the 2D equation can be retrieved, by multiplying it with G and adopting $\overline{\overline{T}} = G \begin{pmatrix} D_{yy} & D_{yE} \\ D_{yE} & D_{EE} \end{pmatrix}$ as the effective diffusion tensor. The retained 2D equation becomes:

$$G\frac{\partial f}{\partial t} = div(\overline{\overline{T}}\nabla f) \tag{3}$$

2.2. The Salammbô model implementation

Salammbô-Electron code has been developed at ONERA since the 90's [6] and coded on FORTRAN. Figure 3 reports the operating scheme of *Salammbô*-Electron where the numerical core plays a central role (central box). It also includes other important branches. They consist in modules for wave-particle interactions [19] or Columbian interactions estimation from which the shape and amplitude of the diffusion coefficients are statistically determined. It also integrates modules taking into account the radiation belts limits and environment such as : Earth's magnetic field or the particle densities at the upper end of the atmosphere. The whole set is parametrized and piloted by proxies and indexes such as *Kp*.

Salammbô's numerical scheme is based on a finite difference 2nd order discretization for space derivation and a first order explicit time integration scheme [10][21]. It uses a logarithmic grid in L^*, a non uniform grid in E

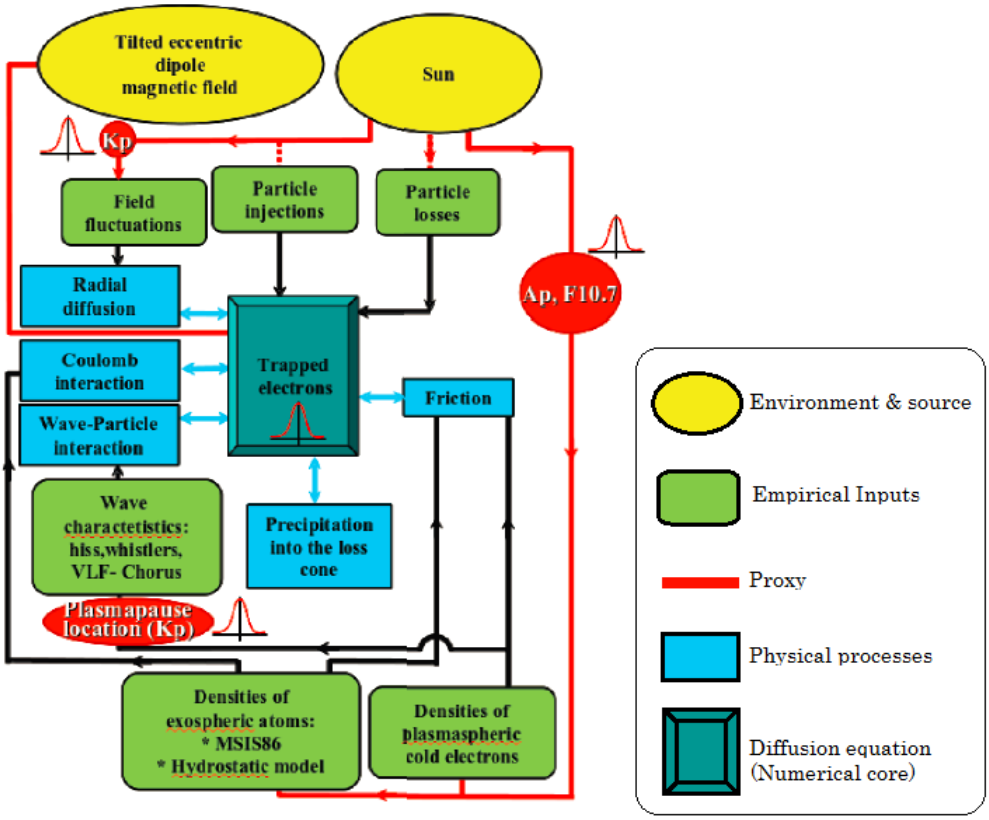

Figure 3: Operating scheme of the Salammbô code for electrons, with its different components and their connections adapted from [20].

with a high refinement at low energy and a non-uniform y grid with a high refinement near $y = 1$ as shown in figure 4. The 3D solving domain can be mapped with a refined grid having $133 \times 49 \times 133$ nodes as well as a reduced grid made of $34 \times 25 \times 34$ nodes and the time steps adopted for each grid is respectively $\Delta t = 5 \cdot 10^{-2} s$ and $\Delta t = 1 s$. In practice, the reduced 3D-grid is the usual adopted grid allowing reasonable computing times. Inputs and coefficients are updated and re-estimated each hour according to the

evolution of the proxies. Cross diffusion DyE terms are omitted for numerical stability considerations [21].

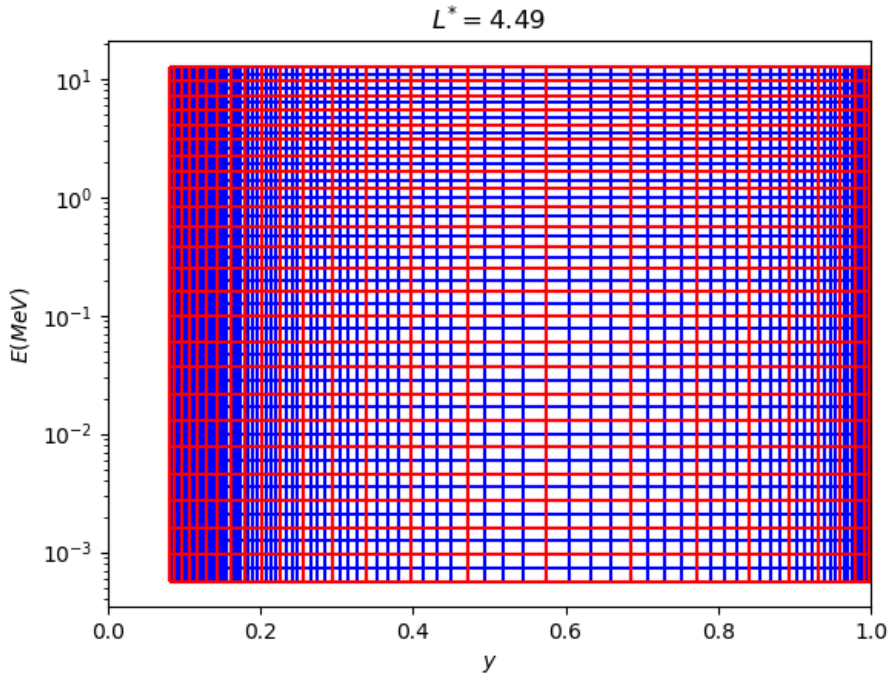

Figure 4: 2D (y,E) finite difference refined (blue) and coarse (red) grids adopted in *Salammbô*-Electron at $L^* = 4.49$.

Table 2 presents the usual boundary conditions adopted in the code, among them the 2D (y, E) plan boundary conditions that will be considered later in this paper.

A reconstruction of the electron radiation belt dynamics at the time-scale of a geomagnetic storm, which is a temporary disruption of the Earth's magnetic field, will require at least 10 days of simulation time, while a solar cycle long evolution requires a simulation time of 11 years to capture the

Table 2: Typical boundary conditions used in *Salammbô*-Electron 3D simulations

Boundary location	Boundary conditions
y_{min}	$f = 0$
y_{max}	$\frac{\partial f}{\partial y} = 0$
E_{min}	$f = g(y, E_{min}, L, t)$ or $\frac{\partial f}{\partial E} = 0$
E_{max}	$f = 0$
$L^*_{min} = 1$	$f = 0$
$L^*_{max} = 8$	$f = h(y, L^*_{max}, t)$

long-term effect of Sun-Earth connection. For information, 1 day simulation with *Salammbô*-Electron on the 3D refined grid requires a time calculation of several hours on a machine with 8Gb RAM memory and a 3.5GHz processor (Serial computing).

Salammbô underwent several incremental improvements to its physical depiction and was validated each time against in situ measurements from satellites and/or empirical models. Especially, it manages to reproduce very well the stationnary state and the dynamic of electron belts during and after a geomagnetic storm with concluding comparison with CRRES satellite measurements [22]. Extensive comparisons with other data have been conducted and results show great consistency of the code with measurements [23]. *Salammbô* also proved its aptitude to evaluate the importance of space plasma trapped wave types and isolate their impact [18][21]. More recently, *Salammbô-Electron* has been upgraded to take into account non-linear losses induced by magnetopause shadowing during severe disturbed periods [11].

2.3. Numerical caveats and limitations seen from Salammbô's scope

As stated before, radiation belts physics involve multi-scale, localized physical processes with different characteristic times and magnitudes. Forcibly, one can observe these local space disparities in the shape taken by the diffusion coefficients and the diffusion tensor in general.

Figure 5 shows the evolution of D_{yy} and D_{EE} in a 2D (y, E) reference space for fixed L^* value to 4.49 and for Kp equal to 6. One can clearly see that D_{yy} and D_{EE} adopt a highly inhomogeneous behaviour. They vary along several orders of magnitude in the logarithmic color bar range. D_{EE} 2D profile shows several narrow sharp resonances around $E = 10^{-2}$ MeV, and a concentric behaviour in the top-right corner at higher E. D_{yy} 2D profile exhibits high stiffness overall, with several trays of high diffusion and a sudden slope near the $y = 1$ boundary. The 2D plots also show a big imbalance in certain regions between the two coefficients, often in favour of D_{yy}, the latter dominating especially the loss cone region at y_{min} and the E_{min} boundary. Moreover, 1D cut plots presented in the same figure, show how the coefficient evolution near the boundaries can adopt radically different behaviours.

Cross diffusion terms D_{yE}, on the other side, reproduce the steepness seen in D_{yy} and D_{EE}. They change sign promptly in certain areas (especially near $y = 1$ and $E = E_{min}$) as it can be seen in Figure 6. If we look closely to the effective full 2D diffusion tensor $\overline{\overline{T}}$ and map its maximum/minimum eigenvalues ratio i.e. the anisotropy ratio at each point in the 2D domain, we can notice high levels of anisotropy that are also unequally distributed. Figure 7 shows for $L^* = 4.49$ a substantial layout of ratios bigger that 10^2, which

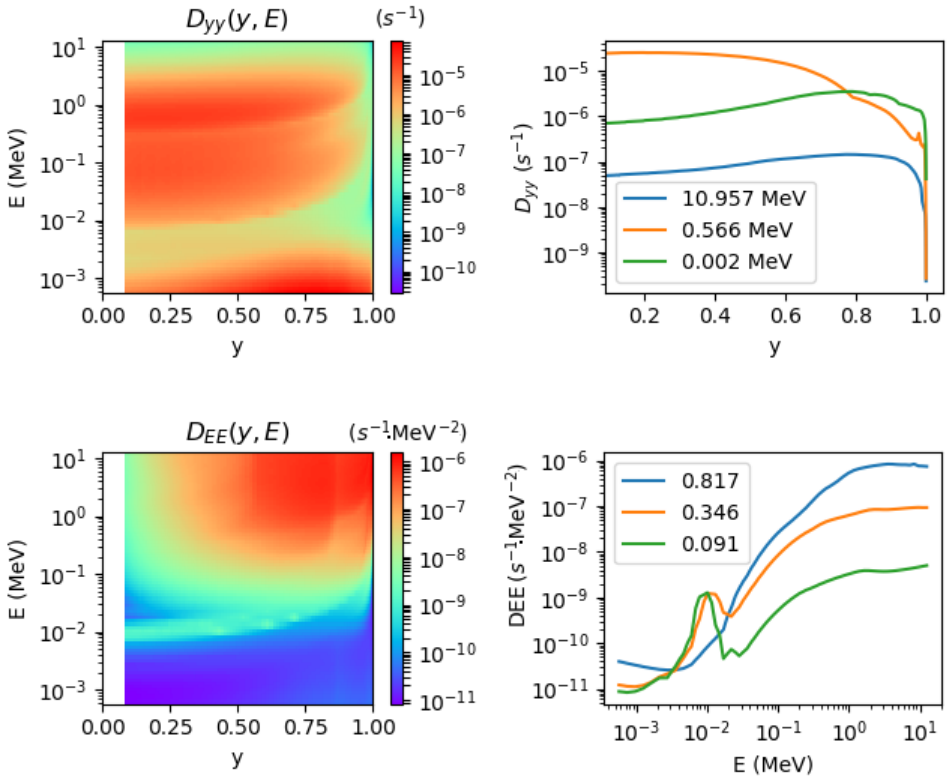

Figure 5: 2D plots and 1D cut plots of D_{yy} and D_{EE} diffusion coefficients at $L^* = 4.49$. 2D plots are represented in the (y, E) space and the 1D plots cut are performed along the diffusion direction of the coefficient at different locations.

represents a significant anisotropy ratio when studying diffusion problems [16] [24]. This ratio is even exceeding 10^7 near $y = 1$ and $E = E_{min}$. In addition to these space evolution particularities, the diffusion tensor is also impacted by the time evolution of the rapidly changing physical processes. Yet, the diffusion tensor form for $Kp = 6$ presented above, can be considered as a worst case.

This form of the diffusion tensor imposes hard constrains on *Salammbô*

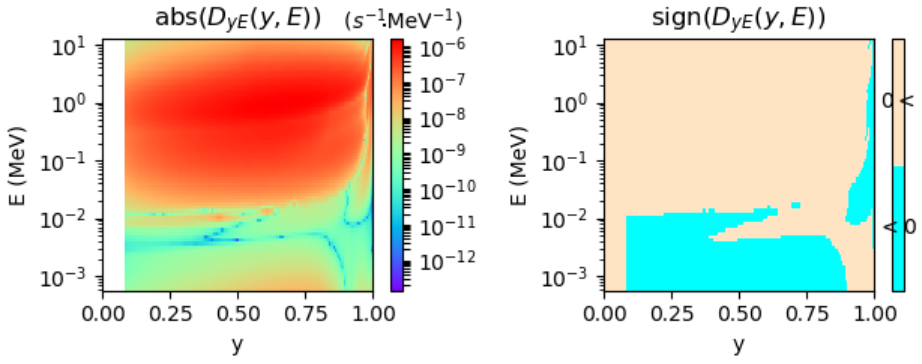

Figure 6: D_{yE} cross diffusion coefficient 2D evolution at $L^* = 4.49$. The right 2D profile reports the absolute value of the coefficient, and the left one shows the sign profile of the coefficient, with cyan for negative and beige for positive values.

numerical resolution. They are reported in the following paragraphs : First, in view of the coefficients spatial inhomogeneity, the finite difference discretization adopted generates numerical instabilities as it evaluates the diffusion coefficient derivatives. Overshoots of the PSD function f are sometimes observed inside areas where the coefficient evolution is steep. Second, the diffusion coefficient amplitude and the small mesh size needed at low E imposes a very restrictive CFL condition for the actual explicit scheme. This results in long calculation times, that comes with other time consuming operations (interpolation, input loading). Besides, the range of very small time steps imposed by the explicit method won't add a substantial gain in precision as the numerical error is largely dominated by the grid error. Last, but not least, cross diffusion presence is an underlined issue. Their presence is subject to discussion [9] and some studies were conducted to evaluate their physical impact [17][25][26][27][28]. However, the radiation belt diffusion community

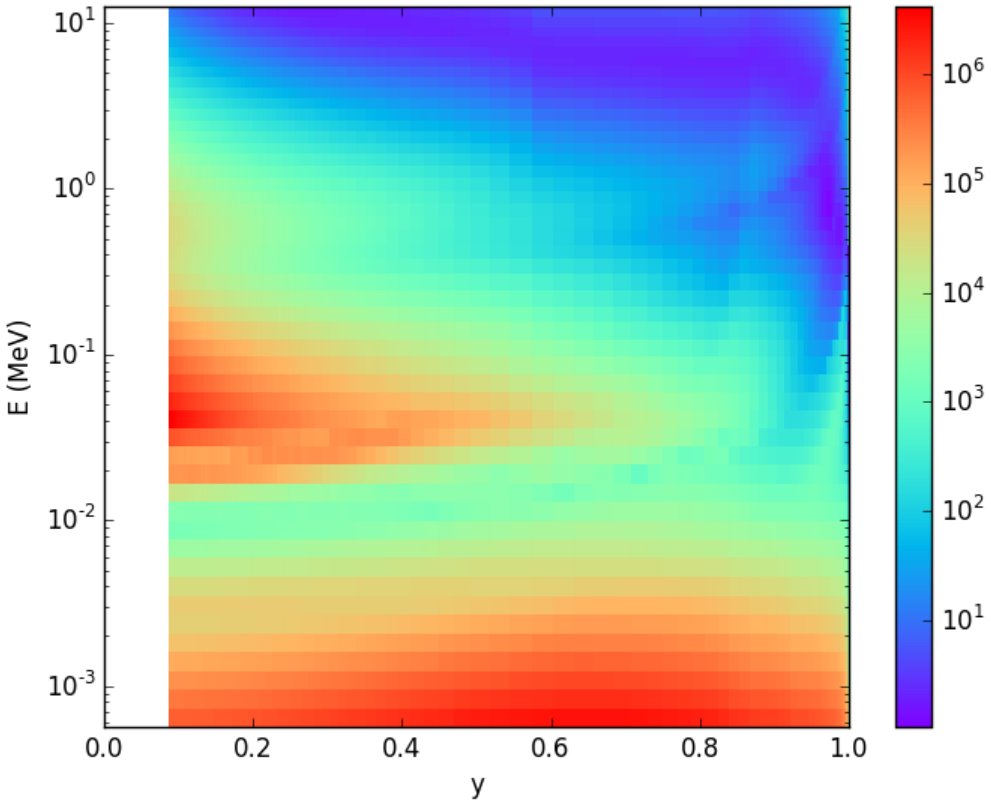

Figure 7: Anisotropy ratio for $L^* = 4.49$

is unanimous as regards to their spurious numerical impact[17][29]. In fact, no clear theoretical stability condition can be properly drawn when they are included in an explicit FD scheme and including them in the current version of *Salammbô*-Electron, will instantly generate numerical instabilities [21]. Until recently, they have been ignored in *Salammbô*'s communicated simulations [18][20][21][23] and in many other model codes [7][9]. As, they are now regaining great care, they have been integrated to several physical codes, advocating for a complete description of the diffusion. Their integration is

conduected by either performing a numerical diagonalization process [17], shifting to a stochastic formulation of the diffusion problem[30], or adopting an implicit/semi-implicit integration [25][27][31]. Yet, cross diffusion terms issue, which can be included in the anisotropy problematic, remains present even when adopting implicit schemes. Indeed, the latter time integration method won't prevent the appearance of negative and non-physical solution values that deteriorates the simulation. In general, typical finite difference methods, even when associated to unconditionnaly stable time integration schemes don't hold an upstream argument preventing this behavior or a strategy to contain its propagation and impact. In that event, the resolution needs the introduction of "ad hoc fixes", that modify locally the solving domain properties to limit these numerical artefacts [12]. Regarding *Salammbô*'s case, we propose exploring a new direction based on finite volume methods, given its promising potential to tackle properly those caveats.

3. Toward a new numerical core for Salammbô

This section presents the steps that we followed to identify the new suitable numerical method. First we list the expected numerical properties to be ensured as regards to our diffusion frame. Then we present the selected FV methods, ensuring the latter properties. Finally we present the results of the numerical tests we conducted to examine their performances.

3.1. Numerical properties expected from schemes solving a typical diffusion problem

We consider the following general steady state diffusion problem :

$$\begin{cases} \nabla \cdot (\overline{\overline{D}} \nabla f) + S = 0 & \text{in } \Omega \\ f = \overline{f} & \text{on } \partial\Omega_1 \\ \boldsymbol{\phi} \cdot \boldsymbol{n} = \overline{\overline{D}} \nabla f \cdot \boldsymbol{n} = 0 & \text{on } \partial\Omega_2 \end{cases} \tag{4}$$

with $\Omega \subset \mathbb{R}^2$ a rectangular domain and $\partial\Omega$ its boundary. $\partial\Omega = \partial\Omega_1 \cup \partial\Omega_2$ is Ω domain frontier, with $\partial\Omega_1$ related to Dirichlet type boundary conditions and $\partial\Omega_2$ related to Neumann boundary conditions. $\boldsymbol{\phi}$ is the boundary flux defined at $\partial\Omega_2$ and $\boldsymbol{n}$ is $\partial\Omega_2$ exterior normal. $S \in L(\Omega^2)$ is the source term and $\overline{\overline{D}}$ a symmetric tensor.

Problem (4) is tied to several mathematical properties that ensure a physically acceptable continuous solution. The **minimum**, **maximum** principles marks off the solution within its values in the boundary [15]

$$\text{For } S = 0 \Rightarrow \inf_{\partial\Omega} \overline{f} \leq f \leq \sup_{\partial\Omega} \overline{f} \tag{5}$$

The **monotony** property, guarantees a physically acceptable positive solution (positivity property) inside the domain Ω [15] :

$$\text{For } S \geq 0 \text{ and } \overline{f} \geq 0 \Rightarrow f \geq 0 \tag{6}$$

On the numerical level, ensuring the discrete formulation of these principles is not straightforward. For instance, in case of high levels of anisotropy (like those we observe in our case), numerical schemes produce numerical solutions with negative values and spurious oscillations [15]. Dealing with this problematic sometimes requires a compromise, depending on the studied application and its requirements [16]. In our case, we considered positivity as the most primordial property to be ensured by the upgraded scheme. The selected scheme must also retain basic numerical standards of consistency

and convergence with a 2nd order convergence rate. The latter properties are automatically extended to the transient problem when they are ensured for the steady state diffusion in (4), with the addition of the initial condition to the limits to be respected.

3.2. Alternative Finite volume methods

Finite volume based methods, are recommended for mass conservation problems [32]. The integration of equation (4) over an elementary volume $K \in \Omega$ yields the local conservation equation.It states the equilibrium in K, between the "volume" creation S and the sum of fluxes $F_{K,\sigma}$ crossing through the interfaces or edges $\sigma \in \partial K$.

$$-\int_{\partial K} \overline{\overline{D}} \nabla f \cdot \boldsymbol{n} dl = \int_K S dV = \sum_{\sigma \in \partial K} F_{K,\sigma} \tag{7}$$

$$F_{K,\sigma} = -\int_\sigma \overline{\overline{D}} \nabla f \cdot \boldsymbol{n}_{\sigma,K} dl \tag{8}$$

$\boldsymbol{n}$ is the normal vector to ∂K, and $\boldsymbol{n}_{\sigma,K}$ is the normal vector to σ edge.

In the finite volume framework, the equation is discretized in a mesh cell and $F_{K,\sigma}$ is approached by a consistent expression. For the rest of the paper, K designates a mesh cell, represented by its center. $K \in T$ with T the set of mesh cells mapping Ω. ε represents the domain boundary edge set. f_K denotes the discrete approximation of f on the K cell, associated with its center. From now on $F_{K,\sigma}$ is merged with its numerical approximation. The FV method offers a significant property specially adapted for conservation laws, which is the conservation of flux :

$$F_{K,\sigma} + F_{L,\sigma} = 0 \tag{9}$$

σ is the edge shared by K and L neighbouring cells.

FV litterature presents many variants of the method. [16] suggest a classification depending on the type of the computed values of the solution f. Cell centred methods such as Linear Two-Points Flux Approximation/TPFA or Linear Multi-Points Flux Approximation/MPFA compute cell center unknowns. Hybrid Mimetic Mixed schemes (HMM), on the other hand compute cell and edge unknowns. Theoretical convergence arguments can be obtained by construction for HMM [15] and conditionally for MPFA [15]. But according to several benchmarks and research works [15][16][24], none of these linear schemes are at least positivity preserving for our anisotropy magnitudes. This is mainly why they were not pre-selected for our investigation.

Non-linear schemes are on the contrary serious candidates [15][16]. We selected for our tests, the monotony preserving Non-Linear Two-Point Flux Approximation scheme, which we will denote as NLTPFA and the Min/Max principles preserving Non-Linear Multi-Point Flux Approximation scheme which we will denote as NLMPFA. We choose to pre-select these two schemes as, unlike linear schemes, non-linear schemes do not ensure equivalence between monotony and Minimum and maximum principles [15].

The main idea of both schemes is based on expressing the discrete flux $F_{K,\sigma}$ through a convex combination of two discrete linear de-centred fluxes F_1 and F_2 expressed on K and L neighbouring cells, sharing the σ edge.

$$F_{K,\sigma} = \mu_1 F_1 - \mu_2 F_2 \tag{10}$$

μ_1 and μ_2 are well defined to preserve flux continuity and genuinely constructed to achieve a property longed for in each scheme.

In case of the NLTPFA, μ_1 and μ_2 are constructed to achieve a two point flux structure :

$$F_{K,\sigma} = \alpha_{K,L}(f) f_L - \beta_{K,L}(f) f_K \tag{11}$$

with $\alpha_{K,L}(f) \geq 0$,$\beta_{K,L}(f) \geq 0$. The equality $\alpha_{K,L}(f) = \beta_{L,K}(f)$ imposed by the flux conservation on σ along with the particular two point structure of the scheme, grants its discretization matrix $\mathbb{M}$ the M-matrix property. Therefore $\mathbb{M}^{-1}$ has only positive entries, and for a positive second member vector, the scheme ensures $f \geq 0$. We followed the development of the method presented in [33] for a polygonal mesh and the special adaptation of the method for a Cartesian grid is presented in Appendix A.

In the NLMPFA scheme, the goal is to express the flux in a multi point structure :

$$F_{K,\sigma} = \sum_M \tau_{K,M}(f_M - f_K) \tag{12}$$

M refers to K's neighbouring cells and $\tau_{K,M} \geq 0$. The multipoint structure (12) is fundamental to preserve extremum principles and the theorem demonstrated in [15][34] proves its ability to prevent internal oscillations inside the domain. We followed the development of the method presented in [34] for a polygonal mesh and the special adaptation of the method for a Cartesian grid is presented in Appendix B.

Picard algorithm method as adopted for both methods in [33][34] is used to solve the non-linear system of equations by following these instructions :
- Initialize f^0
- Loop on n : solve $\mathbb{M}(f^n) f^{n+1} = \mathbb{S}^n$
- Exit loop if residue $||f^{n+1} - f^n|| < \epsilon = 10^{-6}$

3.3. Numerical experiments

To analyse the performance of the latter alternative schemes, several numerical tests or "toy cases" were established. They consist in different configurations of analytical diffusion tensors (gathered in the literature or self-constructed) reproducing real case aspects and include different sets of boundary conditions. These tests also served to verify the prototypes of the new numerical solvers before testing them in real case simulations. In this subsection, we present two numerical studies : the first one focuses on measuring the effect of high levels of anisotropy. We present there 3 different test results related to positivity, the minimum principle and the Min/Max principles. The second numerical study is related to measuring the effect of steep coefficients on accuracy.

We present in the following paragraph, the notations used to present the following numerical results. N_u is the number of cell center unknowns, f_{min} and f_{max}, the extremal values of f inside the solving domain and N_{iter} is the number of non-linear iterations to reach convergence. $Ru = \frac{N_1}{N_u}$ is the ratio of undershoots, with N_1 the number of grid cells where $f_K < 0$ when testing positivity and is equal to the number of grid cells where $f < f_{min}$ when testing the minimum principle preserving property. To evaluate the rate of convergence, we use the discrete counter part of L^2 norm $||.||_2$:

$$||.||_2^D = \sqrt{\sum_{K \in T} f_K^2 m(K)} \tag{13}$$

T is the set of mesh cells, m is the K cell "volume". The relative approxi-

mation error is calculated based on the previously defined norm :

$$Err_2 = 100 \times \frac{||f - f_{ref}||_2^D}{||f_{ref}||_2^D} \tag{14}$$

f_{ref} is the reference solution chosen when evaluating the schemes accuracy by the method of manufactured solution MMS [35]. This method consists in manufacturing a source term for a given function f_{ref} verifying the boundary conditions and a given diffusion tensor. The source term is then computed analytically, knowing the diffusion coefficient and f_{ref} analytical expressions.

All the presented tests were conducted on uniform cartesian grids. To solve non-linear systems, we used picard algorithm. This choice, adopted in [33][34] will preserve monotony of the NLTPFA scheme at each iteration and prevent the appearance of undershoots for the NLMPFA scheme [16] . Initialisation of the non-linear resolution is performed by the solution of a linear finite volume scheme, filtered from overshoots and undershoots. All the numerical tests were conducted using serial codes developed on a Python environment and run on a 12 Gb RAM memory machine with a 2.6 GHz processor. Matrix are filled sparsely and the scipy.sparse package is used for efficient matrix operations and inversions. We used sympy, a symbolic calculation python library to evaluate the analytical expressions of the source term for the MMS method.

3.3.1. Positivity and Min/Max preserving tests

In this primary numerical study, we measure the effect of typical radiation belts anisotropy on NLTPFA and NLMPFA schemes. We established three sub-cases, in which we test both schemes in case of a highly anisotropic analytical tensor. The first one is related to positivity, the second one to

minimum principle preserving and the third one to test Min/Max principles preserving. In each sub-case we measure their computational performances with respect to non-linear convergence and we report the output of a typical 2nd order linear finite difference scheme, to reflect the behaviour of the current *Salammbô* scheme.

In the three studied cases, the diffusion tensor $\overline{\overline{D}}$ is taken as:

$$\frac{1}{x^2+y^2} \cdot \begin{pmatrix} \alpha x^2 + y^2 & (\alpha-1)xy \\ (\alpha-1)xy & x^2 + \alpha y^2 \end{pmatrix} \tag{15}$$

$\overline{\overline{D}}$ has 1 and α as eigenvalues, thus an anisotropy ratio equal to $\frac{1}{\alpha}$ that we choose equal to 10^9. This analytical tensor has also negative coss diffusion terms, same as what one can find in a real case diffusion tensor.

We start with the first, positivity testing case, by adopting the following solving domain $\Omega = [0..1] \times [0..1] \setminus \{(0,0)\}$. We fix a homogeneous Dirichlet condition on $x = 0$,$y = 0$,$y = 1$ and a no-flux boundary at $x = 1$ to reflect typical real boundary conditions of radiation belts models. S adopt the following form :

$$S(x,y) = \begin{cases} 1 \text{ if } (x,y) \in [0.25..0.75] \times [0.25..0.75] \\ 0 \text{ otherwise} \end{cases} \tag{16}$$

Positivity testing results are synthesized in table 3

The f_{min} row in table 3 for NLTPFA and NLMPFA shows how they maintain positivity as expected. For both methods, non-linear convergence is achieved after a relatively high number of iterations. The number of iterations increased for both schemes when the grid was refined. Nonetheless NLTPFA is more competitive than NLMPFA with around 2 times less iter-

Table 3: NLTPFA, NLMPFA and FD results as regards to positivity preserving

Scheme	N_u	20×20	40×40	80×80
NLTPFA	f_{min}	$6.44 \cdot 10^{-10}$	$7.55 \cdot 10^{-15}$	$2.52 \cdot 10^{-23}$
	N_{iter}	81	141	222
NLMPFA	f_{min}	$2.82 \cdot 10^{-7}$	$9.15 \cdot 10^{-10}$	$2.71 \cdot 10^{-13}$
	N_{iter}	153	310	433
FD	f_{min}	-0.00083	-0.00064	-0.00041
	Ru	0.04	0.06	0.05

ations. Other numerical results with higher levels of anisotropy showed that a higher number of non-linear iterations is required to reach convergence. FD results on the other hand confirm the strong limitations of the method to preserve positivity with a typical anisotropy ratio as its f_{min} row reports negative values with not negligible magnitudes. Moreover, the appearance of negative values is not contained as the ratio of negative values Ru increased when the grid was refined.

We switch to the second, minimum preserving test, by adopting a full domain Dirichlet boundary condition $\overline{f} = 1$ on $\partial\Omega$ with the same S term.Minimum preserving testing results are synthesized in table 4

The f_{min} row of NLMPFA in table 4 shows the preservation of the minimum principle by the scheme. NLTPFA results however, shows the opposite, with minimum values under 1. This particular behaviour is expected as minimum principle and monotony are no not equivalent in case of non-linear schemes[15]. Other minimum principle violation cases are also reported in

Table 4: NLTPFA, NLMPFA and FD results as regards to the minimum principle preserving

Scheme	N_u	20×20	40×40	80×80
NLTPFA	f_{min}	0.9983	0.9984	0.9987
	N_{iter}	62	83	66
	Ru	0.1425	0.1431	0.1396
NLMPFA	f_{min}	1.00	1.00	1.00
	N_{iter}	66	107	201
FD	f_{min}	0.9981	0.9983	0.9987
	Ru	0.090	0.127	0.128

[16]. Nevertheless, this issue will not impact our application. In fact, due to the permanent presence of $f = 0$ boundary at y_{min}, the minimum principles implies positivity and so, both properties are the same. Although NLTPFA remains the fastest method, iterations numbers difference between the two methods are not as wide as in the previous sub-case. The previously mentioned behaviour of iterations number increase when the grid is refined, is also observed in this second study. But a small decrease in iteration numbers is observed in NLTPFA when the number of grid cells is quadrupled (from $N_u = 40 \times 40$ to $N_u = 80 \times 80$). This might be explained by our initialization procedure, based a more refined solution. FD results shows the violation of the minimum principle and a consequent ratio of undershoots, increasing when the grid is refined.

For the third, Min/Max preserving test, the solving domain is shrinked

to $\Omega = [0..0.5] \times [0..0.5] \setminus \{(0,0)\}$, $\overline{f} = \sin(\pi x)\sin(\pi y)$ on $x = 0$,$y = 0$,$y = 1$ (Dirichlet condition) and we adopt a no flux condition on $x = 1$ with $S = 0$. Min/Max testing results are synthesized in table 5

Table 5: NLTPFA, NLMPFA and FD results as regards to extremum principles preserving

Scheme	N_u	20×20	40×40	80×80
NLTPFA	f_{min}	$2.22 \cdot 10^{-15}$	$4.67 \cdot 10^{-27}$	$3.60 \cdot 10^{-44}$
	f_{max}	0.9955	0.9988	0.9997
	N_{iter}	95	181	338
NLMPFA	f_{min}	$2.10 \cdot 10^{-9}$	$1.63 \cdot 10^{-13}$	$3.73 \cdot 10^{-18}$
	f_{max}	0.9950	0.9988	0.9995
	N_{iter}	126	250	606
FD	f_{min}	-0.023	-0.021	-0.0187
	f_{max}	0.9872	0.9968	0.9992
	Ru	0.121	0.124	0.132

f_{min} and f_{max} rows in table 5 for both schemes show the preservation of the minimum and the maximum principle. This is expected from the NLMPFA, but achieved with a very high computational cost (over 600 iterations for a 80×80 cells grid). No overshoots were observed in the NLTPFA results, despite this scheme not holding a maximum preserving property [16]. NLTPFA scheme shows a better computational efficiency and thus a better match to our application . The same failure of the FD scheme to tackle anisotropy is also observed in this test case.

3.3.2. Accuracy and precision tests

In the following numerical study, we evaluate the accuracy of both schemes. We measure their precision and convergence rate in case of a steep diagonal diffusion tensor, and in case of the previously used anisotropic diffusion tensor. In both test cases, the solving domain $\Omega = [0..0,5] \times [0..0,5]$ and S is manufactured to have $f_{ref} = \sin(\pi x) \times \sin(\pi y)$ (MMS). The results of the steep coefficients sub-case are synthesized in table 6 and the results of the anisotropic tensor sub-case are synthesized in table 7.

$$\begin{cases} D_{xx} = 10^2 + 10^6 \cdot \exp^{-10x^2} \\ D_{yy} = 10 + 10^3 \cdot \exp^{-2 \cdot 10^2 (y-0.5)^2} \\ D_{yx} = 0 \end{cases} \tag{17}$$

Table 6: Error and convergence rate results for the diagonal inhomogeneous diffusion tensor case

Scheme	N_u	20×20	40×40	80×80
NLTPFA	Err_2	$2.99 \cdot 10^{-1}$	$7.49 \cdot 10^{-2}$	$1.87 \cdot 10^{-2}$
	Order	-	1.99	2.00
NLMPFA	Err_2	$2.99 \cdot 10^{-1}$	$7.49 \cdot 10^{-2}$	$1.87 \cdot 10^{-2}$
	Order	-	1.99	2.00

Table 6 and table 7 results show a 2nd order convergence rates for both schemes. For the diagonal diffusion tensor sub-case, both methods present equal error magnitudes. In case of the full anisotropic tensor, NLTPFA is more precise. For the first two columns, NLMPFA is slightly more competitive than NLTPFA.

Table 7: Error and convergence rate results for the high anisotropy diffusion tensor case

Scheme	N_u	20×20	40×40	80×80
NLTPFA	Err_2	$6.53 \cdot 10^{-2}$	$2.06 \cdot 10^{-2}$	$5.55 \cdot 10^{-3}$
	Order	-	1.66	1.92
	N_{iter}	39	41	21
NLMPFA	Err_2	$3.00 \cdot 10^{-1}$	$7.66 \cdot 10^{-2}$	$1.94 \cdot 10^{-2}$
	Order	-	1.97	1.98
	N_{iter}	32	32	30

4. Transient study results with a real diffusion tensor

We move now to a real physical configuration. As a consequence, the diffusion problem ((4)) is extended to the transient case, the source term is put at zero ($S = 0$) and and we adopt a real life diffusion tensor. In this section we present the results of 2D real life simulations. First, we report a computational cost study of NLTPFA and NLMPFA schemes, both associated to an Euler implicit time integration. Then we evaluate the effect of the FD/FV transition, by comparing a NLTPFA + Euler implicit solver to a FD + Euler explicit solver. Finally, we compare NLTPFA + Euler implicit transient simulations with and without cross diffusion to characterize their effect in the diffusion frame.

All transient simulations, are operated at the $L^* = 4.49$ plane, so that the adopted tensor is the same one presented in section 2.3. It also remains time-independent ($Kp = 6$). We simulate for each case, the diffusion process until $T_{simu} = 90000$ s, starting from a constant initial state $f_{init} = 10^{30}$.

Table 8 presents the limits of our solving domain, as well as the adopted boundary conditions. The 133×49 (y, E) 2D *Salammbô* full grid is used in

Table 8: Boundary conditions used in *Salammbô*-Electron

Boundary location	Boundary conditions
$y_{min} = 0.0862$	$f = 0$
$y_{max} = 1.0$	No-flux boundary
$E_{min} = 5.66 \cdot 10^{-4}$ MeV	$f = 1 \cdot 10^{30}$
$E_{max} = 12.56$ MeV	$f = 0$

FD simulations, from which we generate the FV grid by merging FD nodes with FV grid interfaces.

A convergence study was conducted on both schemes to verify their first order time accuracy using the MMS method with $f_{ref} = \sin(\pi x)\sin(\pi y)\exp(-t)$ with $t_{simu} = 2.0$, for the highly anisotropic diffusion tensor case (15) on a 100×100 uniform grid. The results are reported in table 9.

Table 9: Time order verification for the studied schemes

Scheme	Δt	0.5	0.25	0.125
NLTPFA + Euler implicit	Err_2	1.034	0.469	0.223
	Order	-	1.14	1.073
NLMPFA + Euler implicit	Err_2	1.029	0.468	0.222
	Order	-	1.14	1.073

4.1. NLTPFA and NLMPFA computation cost comparison

For this study case, we conducted several transient simulations with different time steps. We measure the calculation time required for each simulation and the average number of non-linear iterations required for the convergence. NLTPFA scheme converged with all the time steps. But, we observed an odd behaviour from the NLMPFA scheme as it could not reach convergence in some time steps, even after a very high non-linear iteration number (> 500). We observed the oscillation of the residue around a fixed value, when the convergence was not achieved. It was also observed in simulations conducted at other L^* planes. When the no-flux boundary condition at y_{min} is replaced by a homogeneous dirichlet condition, the scheme overcome the oscillatory behaviour. We also considered loosening the residue and the exit criteria of the non-linear algorithm, which allowed the non-linear convergence.

In the table 10, we report the results of the NLTPFA simulations in case of the natural boundary conditions, and the NLMPFA simulations results (denoted as NLMPFA*) when substituting the no-flux boundary conditions at y_{max} with a homogeneous Dirichlet condition, using the same residue formula. N_i is the average number of non-linear iterations, T_c is the calculation time.

One can see, in table 10 that the smaller the time steps are, the smaller non-linear iteration numbers are. In fact, for a smaller Δt, the evolution of the dynamic at each iteration is slower and the change in the numerical solution profile for successive time steps is smaller, thus less non-linear iterations are needed for convergence. For both schemes, the increasing ratio of T_c is not equal to the increasing ratio of the time step. When $\Delta t = 10000s$ is

Table 10: Real case transient results

Scheme	Δt	100s	1000s	10000s
NLTPFA	N_{iter}	7.99	20.98	39.55
	$T_c(s)$	4978.92	1526.67	336.45
NLMPFA*	N_{iter}	19.69	33.18	59.66
	$T_c(s)$	21928.78	4272.83	636.43

divided by 10, T_c is multiplied by around 5 times for NLTPFA and around 7 times for NLMPFA*, making the choice of smaller time steps less cheaper that in linear schemes. Nevertheless, the simulation cost overall, and for the same time step is higher than for a linear scheme, that requires only one iteration per time step.

We observed in the NLTPFA solution profile a violation of the maximum principle with some PSD values exceeding the E_{min} upper limit and the f_{init} initial value. These overshoots are located near the E_{min} limit boundary. We report in figure 8 the evolution of the overshoots ratio in % as function of time, when $\Delta t = 1000s$. We can clearly observe their decrease during the course of the simulation. Regarding their magnitude, they exceeded the maximum by at most three digits for all the NLTPFA simulation.

4.2. FV to FD transition

From now on, we adopt the NLTPFA + Euler implicit solver as the reference solver and we use $\Delta t = 1000s$ as the time integration step. In this section, we compare the latter FV scheme simulation results to those of a FD explicit scheme, representing *Salammbô's* behaviour and coded on the

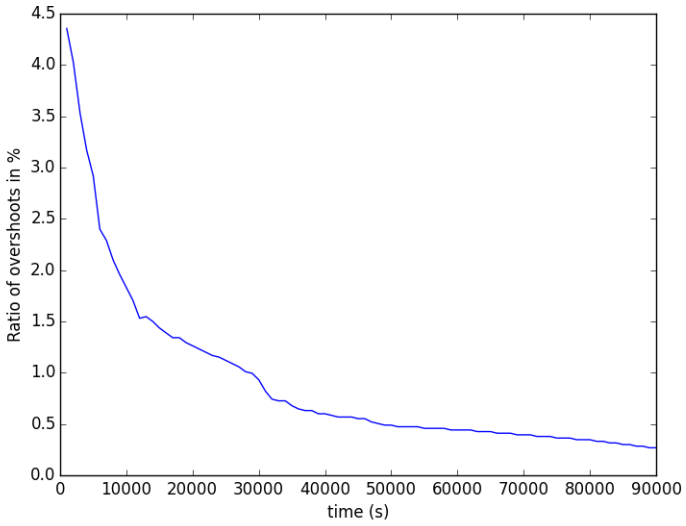

Figure 8: ratio of maximum principle violating points in 2D PSD function profile at $L^* = 4.49$ in function of time, for $\Delta t = 1000s$ using the NLTPFA scheme

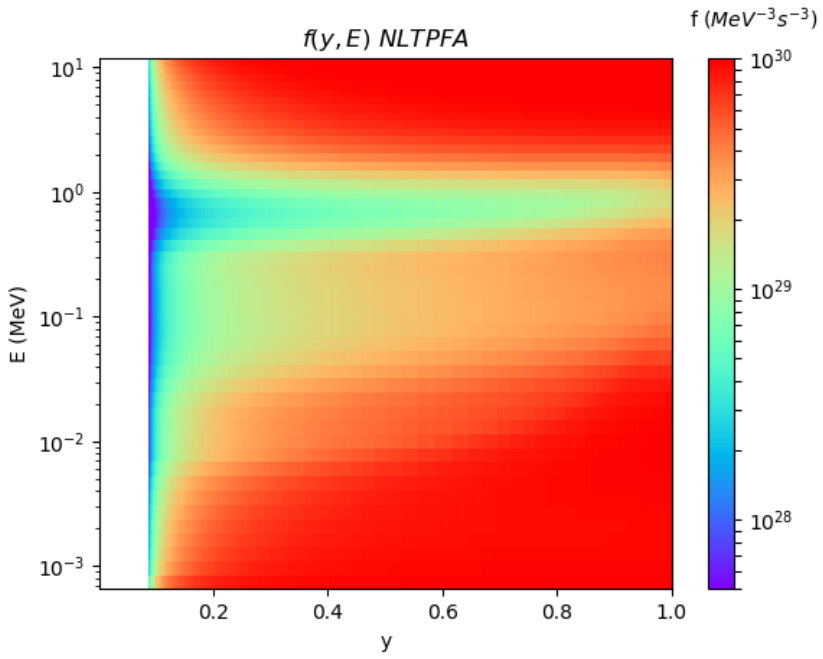

Figure 9: PSD function 2D profile at $L^* = 4.49$ and $T_{simu} = 90000s$ using the NLTPFA scheme

same python environment for the sake of a fair comparison. We used for the explicit simulation a time step of $\Delta t = 50ms$, for which it required $11685s$ of calculation time. Both simulation were operated without cross diffusion terms to compare both solver in the same diffusion frame.

Figure 9 reports the PSD function 2D profile for the NLTPFA scheme, at $t = T_{simu}$ and figure 10 reports the PSD function 2D profile for the FD scheme. We notice that the two 2D profiles are similar. We observe rapidly decaying values near the loss cone at y_{min} on the entire energy direction. A local minimum zone spreads over the entire y direction, around $E = 1MeV$ that merges totally with the D_{yy} maximum zone. The same behaviour is

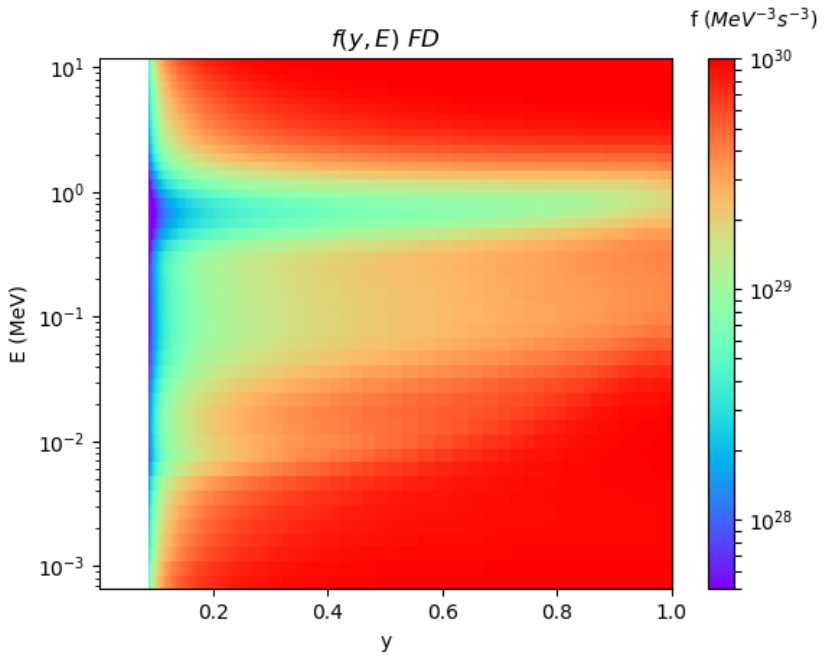

Figure 10: PSD function 2D profile at $L^* = 4.49$ and $T_{simu} = 90000s$ using a finite difference scheme

observed with less importance and on a wider zone, around $E = 0.1$ MeV. The PSD distribution around E_{min} and E_{max} is relatively flat, due to the imbalance between the diffusion directions usually in favour to y.

When looking to their relative difference in figure 11, we see how the diagonal diffusion coefficient steepness is principally driving the difference between the two profiles. This can be seen near $E = 2MeV$, where D_{EE} presents a spread peak. It is also seen in the region located between $(y, E) \in [0.7..0.9] \times [10^{-2}..10^{-1}]$ and at higher energies where D_{yy}. The difference observed at y_{min} originates mainly from the interpolation performed between the finite difference and finite volume grids.

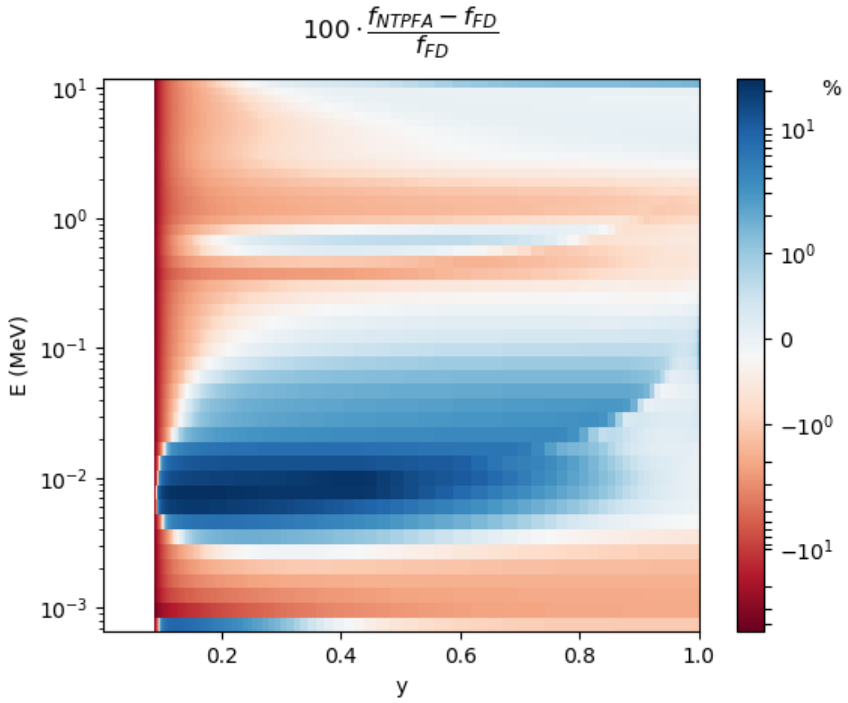

Figure 11: NTPFA and FD relative difference profile at $L^* = 4.49$ and $T_{simu} = 90000s$ without cross diffusion

4.3. Measuring the effect of cross diffusion

As the NLTPFA scheme allows now the full description of the 2D diffusion frame, without a degrading impact on the numerical solution, we are now able to quantify the effect of cross diffusion.

Figure 12 shows the relative difference of the numerical solution for the NLTPFA scheme with and without cross diffusion. Figure 13 reports also 1D cut plots at several energy and pitch angle locations. One can notice that the energy domain located between $E = 10^{-2}$ MeV and $E = 0.6$ MeV for almost all equatorial pitch angles, shows higher PSD magnitude in presence

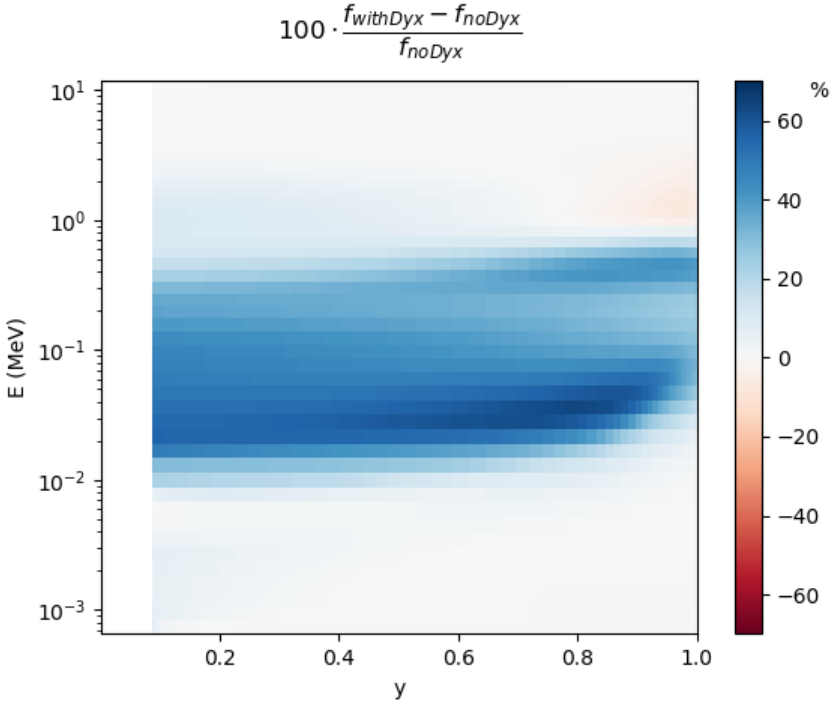

Figure 12: Relative difference profile for the NLTPFA scheme in regards to cross diffusion at $L^* = 4.49$ and $T_{simu} = 90000s$

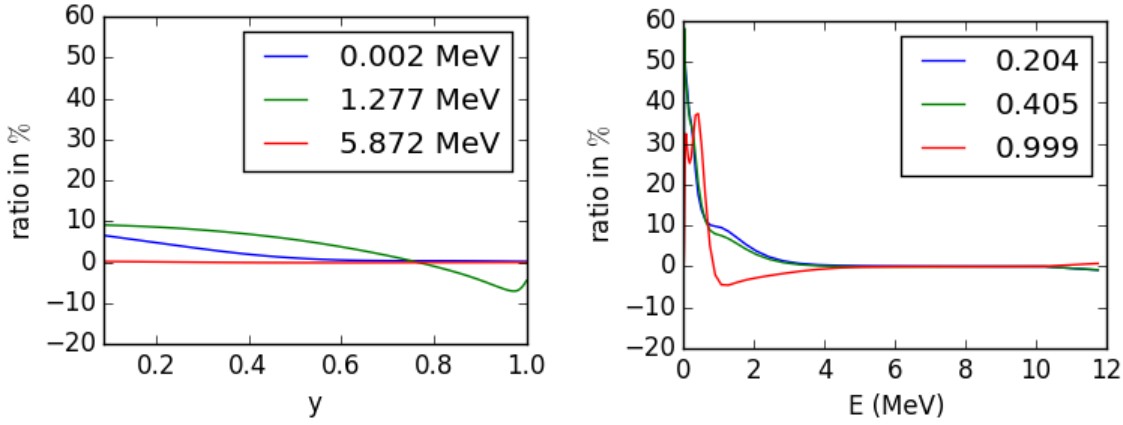

Figure 13: 1D cut plots of the relative error difference for the NLTPFA scheme in regards to cross diffusion at $L^* = 4.49$ and $T_{simu} = 90000s$.

of cross diffusion with relative differences around 60%. This domain is at the radiation belt border and largely influenced by the lower energy boundary. Outside this location, and especially in regions where cross diffusion terms are negative (around the E_{min} boundary), the relative difference stayed at very low levels. We can note that near the $y = 1$ boundary, at $E = 1$ MeV, representing equatorial highly energetic particles, we observe lower PSD magnitudes in presence of the cross diffusion.

5. Summary and conclusion

The prime objective of this investigation was to discuss the complexity of developing a robust and personalized numerical scheme in order to tackle the numerical challenges involved in radiation belts modelling. We presented those challenges originating from our multi-scale physics and embodied by a highly inhomogeneous and anisotropic diffusion tensor.Thus we provide

an interesting field of benchmarking for numerical schemes, in addition to reservoir engineering, radionuclide migration and multiphase flow.

We identified finite volume method alternatives , suitable for our constraints, the NLTPFA scheme and the NLMPFA scheme. They presented satisfying results when tested in real case mimicking analytical tests, with a computational cost advantage to the NLTPFA method. We tested these schemes (associated to an Euler implicit scheme) in case of a real life transient diffusion tensor. Unfortunately NLMPFA was not able to converge. We plan on conducting further studies to identify the reason of this behaviour, while we suspect that the residue formula is too restrictive with respect to our high levels of inhomogeneity. On the other hand the NLTPFA scheme associated to the Euler implicit scheme presented a better performance for a full tensor compared to an explicit finite difference scheme. That's why we choose to adopt it for the new *Salammbô* core, and more specifically to integrate it in the 3D splited transient resolution. Using a finite volume method to solve radiation belts dynamics has not been made so far as well as defining a relevant benchmarking package in our community.

Next step, will consist in optimizing the NLTPFA resolution algorithm as it will be applied in each 2D plan, hence rapidly increasing the computational cost. This optimization is all the more important as *Salammbô* has been associated recently to data assimilation tools requiring several parallel computing loops.

Numerical uncertainties and challenges being put aside, the radiation belt study community still has to master the physical ones, coming from the complex coefficients estimation. In fact, their accuracy may have a noticeable

impact on the solving output and their effects still need to be well estimated and minimized on the equation resolution.

Acknowledgement

This research was supported by CNES, the French space agency and ONERA.

Appendix A. NLTPFA development for a Cartesian grid

We show here, the numerical flux $F_{K,\sigma}$ construction, in the NLTPFA method [33], in case of a full 2D tensor $\overline{\overline{D}} = \begin{pmatrix} D_{xx} & D_{yx} \\ D_{yx} & D_{yy} \end{pmatrix}$ and on a Cartesian mesh (rectangular and conforming), same as for *Salammbô*-Electron mesh.

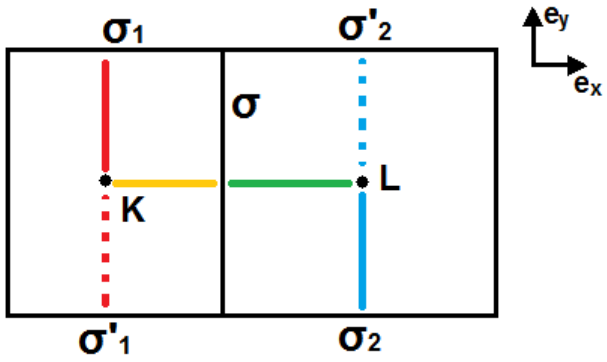

Figure A.14: Construction of NLTPFA stencil on a Cartesian mesh

To express the numerical fluxes F_1 and F_2, we need a discrete expression of the gradient ∇f projected on the $\overline{\overline{D_K}}^T \cdot \boldsymbol{n}_{\sigma,K}$ and $\overline{\overline{D_L}}^T \cdot \boldsymbol{n}_{\sigma,L}$ directions (see ((8)) and knowing that $\overline{\overline{D}}\nabla f \boldsymbol{n} = \nabla f \cdot \overline{\overline{D}}^T \boldsymbol{n}$). $\overline{\overline{D_K}}$ and $\overline{\overline{D_L}}$ are evaluations of the diffusion tensor in K and L.

Considering our rectangular cell case, the direction is expressed in the Cartesian ($\boldsymbol{e}_x$, $\boldsymbol{e}_y$) base reported in the figure A.14, and the projected gradient is evaluated through cell center and edge points, whom sector is crossed by $\overline{\overline{D}}^T \boldsymbol{n}_{\sigma,K}$ and $\overline{\overline{D}}^T \boldsymbol{n}_{\sigma,L}$ respectively for F_1 and F_2.

In the end, and in our special Cartesian case, the expression of F_1 and F_2 will depend on the sign of D_{yx} in each cell. Thereby we have :

$$\begin{cases} F_1 = D_{xx}(K) \cdot \frac{f_\sigma - f_K}{x_\sigma - x_K} + D_{yx}(K) \cdot \frac{f_{\sigma_1} - f_K}{y_{\sigma_1} - y_K} \text{ if } D_{yx}(K) \geq 0 \\ \text{or} \\ F_1 = D_{xx}(K) \cdot \frac{f_\sigma - f_K}{x_\sigma - x_K} + D_{yx}(K) \cdot \frac{f_K - f_{\sigma'_1}}{y_K - y_{\sigma'_1}} \text{ if } D_{yx}(K) < 0 \end{cases} \tag{A.1}$$

and

$$\begin{cases} F_2 = -D_{xx}(L) \cdot \frac{f_L - f_\sigma}{x_L - x_\sigma} - D_{yx}(L) \cdot \frac{f_L - f_{\sigma_2}}{y_L - y_{\sigma_2}} \text{ if } D_{yx}(L) \geq 0 \\ \text{or} \\ F_2 = -D_{xx}(L) \cdot \frac{f_L - f_\sigma}{x_L - x_\sigma} - D_{yx}(L) \cdot \frac{f_{\sigma'_2} - f_L}{y\sigma'_2 - y_L} \text{ if } D_{yx}(L) < 0 \end{cases} \tag{A.2}$$

As represented in figure A.14, the solid yellow and solid green segments embody the gradient projection on the diagonal direction or the normal direction of the studied edge. While the solid blue and solid red segments are related to the off diagonal direction in case of a positive cross diffusion term. Their dashed counter parts are related to the case where cross diffusion is negative.

Getting back to the general development of the method as shown in [33], to get to the two point approximation as presented in ((11)), ((A.1)) and ((A.2)) expressions are injected in ((10)) then cell centred terms and edge terms are regrouped separately:

$$F_{K,\sigma} = \alpha f_L - \beta f_K + a_1(f)\mu_1 - a_2(f)\mu_2 \tag{A.3}$$

where a_1 and a_2 contain edge terms and we impose $a_1(f)\mu_1 - a_2(f)\mu_2 = 0$. μ_1 and μ_2 are then computed based on this system :

$$\begin{cases} a_1\mu_1 - a_2\mu_2 = 0 \\ \mu_1 + \mu_2 = 1 \end{cases} \tag{A.4}$$

Thus

$$\begin{cases} \mu_1 = \frac{a_2}{a_1+a_2} \\ \mu_2 = \frac{a_1}{a_1+a_2} \end{cases} \text{ if } a_1 + a_2 \neq 0 \text{ else } \mu_1 = \mu_2 = 0.5 \tag{A.5}$$

Edge values intervening in a_1 and a_2 expression are interpolated from cell unknowns.

Appendix B. NLMPFA development for a Cartesian grid

To achieve the NLMPFA form, we start from the expression of F_1 and F_2 previously defined and replace edge values directly with convex combination of neighbouring cell unknowns. For instance :

$$f_\sigma = \frac{x_L - x_\sigma}{x_L - x_K} f_K + \frac{x_\sigma - x_K}{x_L - x_K} f_L \tag{B.1}$$

Thereby (A.1) and (A.2) are expressed in the Cartesian grid reported in the figure B.15 as follows :

$$\begin{cases} F_1 = D_{xx}(K) \cdot \frac{f_L - f_K}{x_L - x_K} + D_{yx}(K) \cdot \frac{f_{M_1} - f_K}{y_{M_1} - y_K} \text{ if } D_{yx}(K) \geq 0 \\ \text{or} \\ F_1 = D_{xx}(K) \cdot \frac{f_L - f_K}{x_L - x_K} + D_{yx}(K) \cdot \frac{f_K - f_{M_2}}{y_K - y_{M_2}} \text{ if } D_{yx}(K) < 0 \end{cases} \tag{B.2}$$

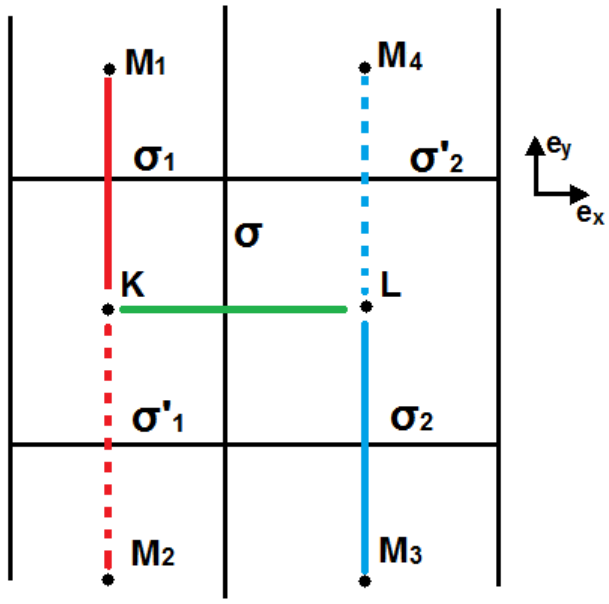

Figure B.15: Construction of NLMPFA stencil on a rectangular conforming mesh

and

$$\begin{cases} F_2 = -D_{xx}(L) \cdot \frac{f_L - f_K}{x_L - x_K} - D_{yx}(L) \cdot \frac{f_L - f_{M_3}}{y_L - y_{M_3}} \text{ if } D_{yx}(L) \geq 0 \\ \text{or} \\ F_2 = -D_{xx}(L) \cdot \frac{f_L - f_K}{x_L - x_K} - D_{yx}(L) \cdot \frac{f_{M_4} - f_L}{y_{M_4} - y_L} \text{ if } D_{yx}(L) < 0 \end{cases} \tag{B.3}$$

As represented in figure B.15, the solid green segment embody the gradient projection on the diagonal direction or the normal direction of the studied edge. While the solid blue and red segments are related to the off diagonal direction in case of a positive cross diffusion terms. Their dashed counter parts are related to the case where cross diffusion is negative.

F_1 and F_2 can then be expressed according to this multipoint form :

$$\begin{cases} F_1 = \sum_M \nu^1_{K,M}(f_M - f_K) \\ F_2 = \sum_M \nu^2_{K,M}(f_M - f_L) \end{cases} \tag{B.4}$$

With M neighbouring cells of the studied cell i.e: L,M_1 or M_2 (depending on the sign of $D_{yx}(K)$) for F_1 and K, M_3 or M_4 (depending on the sign of $D_{yx}(L)$) for F_2. Getting back to the general development of the method as shown in [34] and to ensure ((9)), μ_1 and μ_2 are chosen depending on the sign of F_1 and F_2 :

- if $F_1F_2 \leq 0$:

$$\begin{cases} \mu_1 = \frac{|F_2|}{|F_1|+|F_2|} \\ \mu_2 = \frac{|F_1|}{|F_1|+|F_2|} \end{cases} \text{ if } |F_1| + |F_2| \neq 0 \text{ else } \mu_1 = \mu_2 = 0.5 \tag{B.5}$$

making $F_{K,\sigma} = 2\mu_1 F_1$.

- if $F_1F_2 > 0$ then we define sub-fluxes G_1 and G_2 such as :

$$\begin{cases} F_1 = \lambda^1(f_L - f_K) + \underbrace{\sum_{M \neq L} \nu^1_{K,M}(f_M - f_K)}_{G_1} \\ F_2 = \lambda^2(f_K - f_L) + \underbrace{\sum_{M \neq K} \nu^2_{K,M}(f_M - f_L)}_{G_2} \end{cases} \tag{B.6}$$

With this new configuration and depending on the sign of G_1 and G_2 we have : - if $G_1G_2 > 0$ then $F_{K,\sigma} = (\mu_1\lambda^1 + \mu_2\lambda^2)(f_L - f_K)$

- if $G_1G_2 \leq 0$ then $F_{K,\sigma} = (\mu_1\lambda^1 + \mu_2\lambda^2)(f_L - f_K) + 2\mu_1 G_1$

$$\begin{cases} \mu_1 = \frac{|G_2|}{|G_1|+|G_2|} \\ \mu_2 = \frac{|G_1|}{|G_1|+|G_2|} \end{cases} \text{ if } |G_1| + |G_2| \neq 0 \text{ else } \mu_1 = \mu_2 = 0.5 \tag{B.7}$$

The multipoint structure ((12)) is fundamental to preserve extremum principles and the theorem demonstrated in [34] proves its ability to prevent internal oscillations inside the domain.

References

[1] M. K. Hudson, B. T. Kress, M. H. R., J. A. Zastrow, J. B. Blake, Relationship of the van allen radiation belts to solar wind drivers, Journal of Atmospheric and Solar-Terrestrial Physics 70 (5) (2008) 708 – 729. doi:https://doi.org/10.1016/j.jastp.2007.11.003.

[2] R. B. Horne, S. A. Glauert, N. P. Meredith, D. Boscher, V. Maget, D. Heynderickx, D. Pitchford, Space weather impacts on satellites and forecasting the earth's electron radiation belts with spacecast, Space Weather 11 (4) (2013) 169–186. doi:10.1002/swe.20023.

[3] S. Bourdarie, V. Maget, R. Friedel, D. Boscher, A. Sicard, D. Lazaro, "complementarity of measurements and models in reproducing earth's radiation belt dynamics", in: J. "Lilensten (Ed.), "Space Weather : Research Towards Applications in Europe", Springer Netherlands, "2007", pp. "219–229".

[4] M. Schulz, L. J. Lanzerotti, Particle diffusion in the radiation belts, Physics and chemistry in space, Springer-Verlag, 1974.

[5] J. Roederer, H. Zhang, Dynamics of Magnetically Trapped Particles: Foundations of the Physics of Radiation Belts and Space Plasmas, 2014. doi:10.1007/978-3-642-41530-2.

[6] T. Beutier, D. Boscher, A three-dimensional analysis of the electron radiation belt by the salammbô code, Journal of Geophysical Research: Space Physics 100 (A8) (1995) 14853–14861. doi:10.1029/94JA03066.

[7] D. A. Subbotin, Y. Y. Shprits, Three-dimensional modeling of the radiation belts using the versatile electron radiation belt (verb) code, Space Weather 7 (10) (2009). doi:10.1029/2008SW000452.

[8] Z. Su, F. Xiao, H. Zheng, S. Wang, Steerb: A three-dimensional code for storm-time evolution of electron radiation belt, Journal of Geophysical Research: Space Physics 115 (A9) (2010). doi:10.1029/2009JA015210.

[9] S. A. Glauert, R. B. Horne, N. P. Meredith, Three-dimensional electron radiation belt simulations using the bas radiation belt model with new diffusion models for chorus, plasmaspheric hiss, and lightning-generated whistlers, Journal of Geophysical Research: Space Physics 119 (1) (2014) 268–289. doi:10.1002/2013JA019281.

[10] S. A. Bourdarie, V. Maget, Electron radiation belt data assimilation with an ensemble kalman filter relying on the salammbô code, Annales Geophysicae 30 (2012) 929. doi:10.5194/angeo-30-929-2012.

[11] D. Herrera, V. F. Maget, A. Sicard-Piet, Characterizing magnetopause shadowing effects in the outer electron radiation belt during geomagnetic storms, Journal of Geophysical Research: Space Physics 121 (10) (2016) 9517–9530. doi:10.1002/2016JA022825.

[12] J. M. Albert, Comment on "on the numerical simulation of particle dynamics in the radiation belt. part i: Implicit and semi-implicit schemes"

and “on the numerical simulation of particle dynamics in the radiation belt. part ii: Procedure based on the diagonalization of the diffusion tensor” by e. camporeale et al., Journal of Geophysical Research: Space Physics 118 (12) (2013) 7762–7764. doi:10.1002/2013JA019126.

[13] E. L. Wilson, R. E. Nickell, Application of the finite element method to heat conduction analysis, Nuclear engineering and design 4 (3) (1966) 276–286.

[14] V. Thomée, Galerkin finite element methods for parabolic problems, Vol. 1054, Springer, 1984.

[15] J. Droniou, Finite volume schemes for diffusion equations: introduction to and review of modern methods, Mathematical Models and Methods in Applied Sciences 24 (8) (2014) 1575 – 1619. doi:10.1142/S0218202514400041.

[16] M. Schneider, D. Gläser, B. Flemisch, R. Helmig, Comparison of finite-volume schemes for diffusion problems, Oil Gas Sci. Technol. - Rev. IFP Energies nouvelles 73 (2018) 82. doi:10.2516/ogst/2018064.

[17] J. M. Albert, S. L. Young, Multidimensional quasi-linear diffusion of radiation belt electrons, Geophysical Research Letters 32 (14) (2005). doi:10.1029/2005GL023191.

[18] A. Varotsou, D. Boscher, S. Bourdarie, R. B. Horne, S. A. Glauert, N. P. Meredith, Simulation of the outer radiation belt electrons near geosynchronous orbit including both radial diffusion and resonant interaction

with whistler-mode chorus waves, Geophysical Research Letters 32 (19) (2005). doi:10.1029/2005GL023282.

[19] A. Sicard-Piet, D. Boscher, S. Bourdarie, Wapi : A new model for the wave particle interaction (01 2008).

[20] V. Maget, S. Bourdarie, D. Boscher, R. H. W. Friedel, Data assimilation of lanl satellite data into the salammbô electron code over a complete solar cycle by direct insertion, Space Weather 5 (10) (2007).

[21] A. Varotsou, D. Boscher, S. Bourdarie, R. B. Horne, N. P. Meredith, S. A. Glauert, R. H. Friedel, Three-dimensional test simulations of the outer radiation belt electron dynamics including electron-chorus resonant interactions, Journal of Geophysical Research: Space Physics 113 (A12) (2008). doi:10.1029/2007JA012862.

[22] S. Bourdarie, D. Boscher, T. Beutier, J. A. Sauvaud, M. Blanc, Magnetic storm modeling in the earth's electron belt by the salammbô code, Journal of Geophysical Research: Space Physics 101 (A12) (1996) 27171–27176. doi:10.1029/96JA02284.

[23] S. Bourdarie, R. H. W. Friedel, J. Fennell, S. Kanekal, T. E. Cayton, Radiation belt representation of the energetic electron environment: Model and data synthesis using the salammbô radiation belt transport code and los alamos geosynchronous and gps energetic particle data, Space Weather 3 (4) (2005). doi:10.1029/2004SW000065.

[24] R. Herbin, F. Hubert, Benchmark on Discretization Schemes for Anisotropic Diffusion Problems on General Grids, in: ISTE (Ed.), Finite

volumes for complex applications V, Wiley, France, 2008, pp. 659–692. URL https://hal.archives-ouvertes.fr/hal-00429843

[25] D. Subbotin, Y. Shprits, B. Ni, Three-dimensional verb radiation belt simulations including mixed diffusion, Journal of Geophysical Research: Space Physics 115 (A3) (2010). doi:10.1029/2009JA015070.

[26] X. Tao, A. A. Chan, J. M. Albert, J. A. Miller, Stochastic modeling of multidimensional diffusion in the radiation belts, Journal of Geophysical Research: Space Physics (1978–2012) 113 (A7) (7 2008).

[27] F. Xiao, Z. Su, H. Zheng, S. Wang, Modeling of outer radiation belt electrons by multidimensional diffusion process, Journal of Geophysical Research: Space Physics 114 (A3) (2009). doi:10.1029/2008JA013580.

[28] Z. Su, H. Zheng, L. Chen, S. Wang, Numerical simulations of storm-time outer radiation belt dynamics by wave–particle interactions including cross diffusion, Journal of Atmospheric and Solar-Terrestrial Physics 73 (1) (2011) 95 – 105.

[29] J. M. Albert, Using quasi-linear diffusion to model acceleration and loss from wave-particle interactions, Space Weather 2 (9) (9 2004).

[30] X. Tao, J. M. Albert, A. A. Chan, Numerical modeling of multidimensional diffusion in the radiation belts using layer methods, Journal of Geophysical Research: Space Physics 114 (A2) (2009). doi:10.1029/2008JA013826.

[31] E. Camporeale, G. Delzanno, S. Zaharia, J. Koller, On the numerical simulation of particle dynamics in the radiation belt: 2. procedure based

on the diagonalization of the diffusion tensor, Journal of Geophysical Research: Space Physics 118 (06 2013). doi:10.1002/jgra.50278.

[32] R. Eymard, T. Gallouët, R. Herbin, Finite volume methods, Handbook of numerical analysis 7 (2000) 713–1018.

[33] Y. Guangwei, S. Zhiqiang, Monotone finite volume schemes for diffusion equations on polygonal meshes, Journal of Computational Physics 227 (12) (2008) 6288 – 6312. doi:https://doi.org/10.1016/j.jcp.2008.03.007.

[34] S. Zhiqiang, Y. Guangwei, The finite volume scheme preserving extremum principle for diffusion equations on polygonal meshes, Journal of Computational Physics 230 (7) (2011) 2588 – 2604. doi:https://doi.org/10.1016/j.jcp.2010.12.037.

[35] K. Salari, P. Knupp, Code verification by the method of manufactured solutions (6 2000). doi:10.2172/759450.